Doping-dependent correlation effects in $(Sr_{1-x}La_x)_3Ir_2O_7$

Gregory Affeldt,[1,2] Tom Hogan,[3,4] Jonathan D. Denlinger,[5] Ashvin Vishwanath,[1,2] Stephen D. Wilson,[6] and Alessandra Lanzara[1,2]

[1]*Materials Sciences Division, Lawrence Berkeley National Laboratory, Berkeley, California 94720, USA*
[2]*Department of Physics, University of California, Berkeley, California 94720, USA*
[3]*Department of Physics, Boston College, Boston, Massachusetts 02467, USA*
[4]*Materials Department, University of California, Santa Barbara, California 93106, USA*
[5]*Advanced Light Source, Lawrence Berkeley National Laboratory, Berkeley, California 94720, USA*
[6]*Materials Department, University of California Santa Barbara, Santa Barbara, California 93106, USA*

(Received 26 August 2017; revised manuscript received 30 November 2017; published 9 March 2018)

We have measured the signatures of electronic energy scales and their doping evolution in the band structure of $(Sr_{1-x}La_x)_3Ir_2O_7$ using angle-resolved photoemission spectroscopy. While band splittings and positions corresponding to the bilayer splitting and spin-orbit coupling undergo only small changes, the Mott gap and effective mass of both the lower Hubbard band and conduction band exhibit strong variations with doping. These changes correspond to similar observations in the cuprate superconductors, and are likely connected to the changing effective Coulomb interaction upon addition of itinerant carriers.

DOI: 10.1103/PhysRevB.97.125111

I. INTRODUCTION

Much recent progress has been made in understanding the nature of the spin-orbit Mott state in the layered perovskite iridates [1–15], in which spin-orbit coupling and Coulomb electron-electron correlations combine to form an insulating state. The spin-orbit coupling arranges the t_{2g} bands by an effective angular momentum into a filled $J_{\text{eff}} = \frac{3}{2}$ state and a half-filled $J_{\text{eff}} = \frac{1}{2}$ state. The Coulomb correlation is sufficient to localize the $J_{\text{eff}} = \frac{1}{2}$ electrons in a Mott state, with Mott-like gaps observed in both the single-layer Sr_2IrO_4 [1] and the the bilayer $Sr_3Ir_2O_7$ [6,9]. When the former is doped with electrons, either via La substitution on the Sr site [16] or via the surface deposition of potassium atoms [14], band structures highly similar to the cuprates emerge with Fermi arcs, pseudogaps, and evidence of a d-wave gap that may be indicative of superconductivity in the case of the potassium surface doping [13,17]. Hole doping in $Sr_2Ir_{1-x}Rh_xO_4$ is also reported to establish Fermi arc and pseudogap states, though with a markedly different Fermi surface [18]. These and other related observations have lent additional credence to the notion that pseudogap phases arise essentially from the physics of a doped Mott insulator.

Bilayer $Sr_3Ir_2O_7$ exhibits several important differences from the single layer Sr_2IrO_4. In addition to its larger bandwidth and smaller Mott gap, the magnetic moments in the antiferromagnetic state in $Sr_3Ir_2O_7$ align along the crystallographic c axis [2] (rather than in the ab plane as in Sr_2IrO_4 [19] and the cuprates), and the magnetic excitation spectrum exhibits a large magnon gap [4]. Upon doping in $(Sr_{1-x}La_x)_3Ir_2O_7$, the parent antiferromagnetic insulating state gives way to a paramagnetic metallic state near $x = 4\%$ [11,20] with short-range antiferromagnetic correlations persisting out to at least $x = 6.5\%$ [21]. No signatures of superconductivity have been reported in this system. Additionally, it exhibits small electronlike Fermi-surface pockets and a low-energy suppression of spectral weight in the antiferromagnetic state [22] instead of the large holelike Fermi surface with anisotropic pseudogap and Fermi arcs in Sr_2IrO_4. A recent ultrafast reflectivity study has also revealed a charge-density-wave-like instability in the metallic regime [23] that may be connected to a structural distortion observed via x-ray scattering, suggesting that charge-lattice interactions also play an important role in $(Sr_{1-x}La_x)_3Ir_2O_7$ [11].

Here we present a doping-dependent study of the electronic structure of electron-doped $(Sr_{1-x}La_x)_3Ir_2O_7$ ($0.01 \leqslant x \leqslant 0.06$) using angle-resolved photoemission spectroscopy (ARPES). As doping increases, the Mott gap decreases and an electronlike conduction band appears near the M point. These changes are accompanied by a shift of the band structure beyond a simple rigid-shift picture of doping, including an increase of the effective mass of both the conduction band and lower Hubbard band. In contrast, band splittings related to both the bilayer interaction and spin-orbit coupling are nearly constant with doping. These results mirror previous observations in the cuprates and other transition-metal oxides near the Mott state, suggesting a similar role of Mott physics in this system.

II. EXPERIMENTAL DETAILS

Single-crystal samples of $(Sr_{1-x}La_x)_3Ir_2O_7$ were synthesized using a flux method as described elsewhere [11]. ARPES measurements were performed at beamlines 4.0.3 and 10.0.1 of the Advanced Light Source at temperatures ranging from 15 to 240 K. The samples were cleaved *in situ* and measured at pressures better than 6×10^{-11} Torr. The chemical potential was referenced to a polycrystalline gold surface evaporated *in situ* on the sample puck for measurements at beamline 4.0.3 or a separate calibrating gold film sample with identical beamline configuration at ALS beamline 10.0.1.

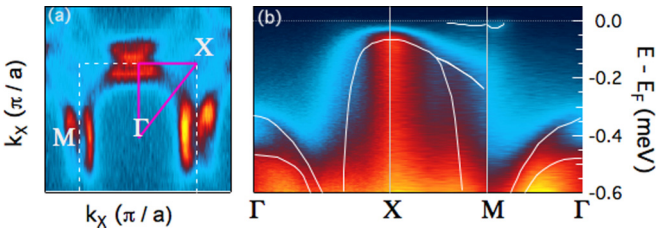

FIG. 1. Fermi surface and dispersion in $(Sr_{0.94}La_{0.06})_3Ir_2O_7$. (a) Fermi surface of the $x = 6\%$ sample. The white dashed square is the boundary of the reduced Brillouin zone (BZ). (b) Energy-momentum distribution of ARPES intensity along high-symmetry directions in the first Brillouin zone. White curves are guides to the eye for the band dispersions.

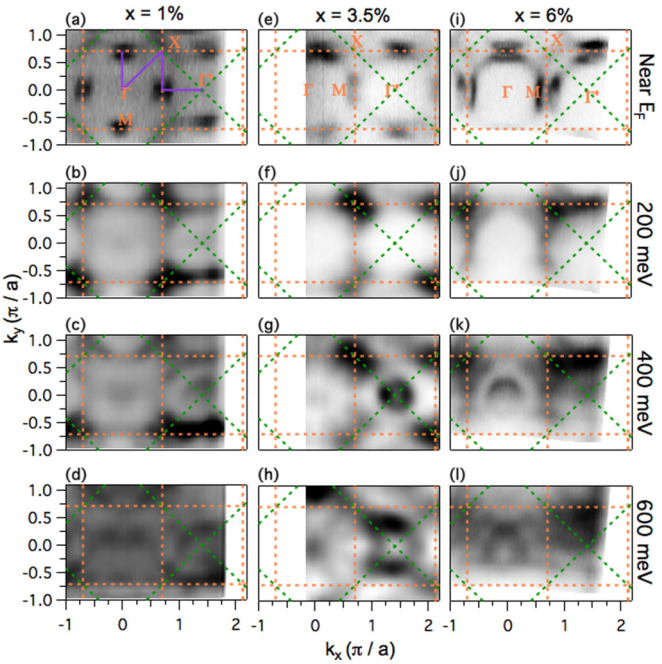

FIG. 2. Constant energy maps for $x = 1\%$ (a)–(d), $x = 3.5\%$ (e)–(h), and $x = 6\%$ (i)–(l) samples at binding energies from 0 to 600 meV. The orange dashed square represents the Brillouin zone of $Sr_3Ir_2O_7$ while the green dashed squares represent the Brillouin zone when the unit cell doubling due to Ir-O octahedral rotations is ignored.

III. RESULTS

The experimental ARPES signatures of electronic correlations studied in this paper are illustrated in Fig. 1 for a metallic $(Sr_{0.94}La_{0.06})_3Ir_2O_7$ ($x = 6\%$) sample. The low-energy dispersion is seen in the energy-momentum cut in Fig. 1(b) along high-symmetry directions in the first Brillouin zone. White curves are guides to the eye for the dispersion of the four bands visible in this energy window. The small electronlike bands near the M point give rise to the lens-shaped Fermi surface seen in Fig. 1(a). Local density approximation calculations including spin-orbit coupling and on-site Coulomb repulsion (LDA+SOC+U) show the minimum of the upper Hubbard band near the M point, but whether the band observed in ARPES is the upper Hubbard band or an in-gap state remains to be conclusively determined. Since in the more heavily doped samples this band crosses the Fermi level, we follow previous ARPES works [24–26] in referring to it as the "conduction band" independent of its origin. The holelike band near the X point is identified as the lower Hubbard band, following works on undoped $Sr_3Ir_2O_7$ [9,27]. The band maxima at Γ are commonly attributed to the $J_{\text{eff}} = \frac{3}{2}$ bands [9,27,28], and their separation is due to the bilayer splitting present in $Sr_3Ir_2O_7$.

Figure 2 shows constant energy maps of the ARPES intensity from lightly doped ($x = 1\%$) through a doping near the metal-insulator transition ($x = 3.5\%$) to heavily doped ($x = 6\%$) $(Sr_{1-x}La_x)_3Ir_2O_7$ samples. The orange dashed lines represent the boundaries of the surface Brillouin zone in the presence of either AF order or the unit cell doubling generated by the staggered rotation of Ir-O octahedra, while the green dashed lines are the boundaries of the unreduced Brillouin zone. Γ here denotes the momentum coming from normal emission of photoelectrons. Γ′ is equivalent to Γ in the reduced Brillouin zone but represents a distinct crystal momentum in the larger zone. The Fermi surface for each is shown in panels (a), (e), and (i) and consists of electronlike pockets near the M point along the boundary of the reduced Brillouin zone. While these pockets are well separated in the $x = 1\%$ sample, the increased pocket size in the $x = 6\%$ sample leads to significant deviation from an elliptical shape and hybridization between adjacent pockets near the $\Gamma - X$ direction as well as along the Brillouin-zone boundary. These bands are absent at a binding energy of 200 meV, shown in panels (b), (f), and (j), where the primary spectral weight arises from the $J_{\text{eff}} = \frac{1}{2}$ lower Hubbard band at the X point. At a binding energy of 400 meV, the $J_{\text{eff}} = \frac{3}{2}$ bands at Γ/Γ′ are visible along with the $J_{\text{eff}} = \frac{1}{2}$ lower Hubbard band near X. At 600 meV, most bands should be of mostly $J_{\text{eff}} = \frac{3}{2}$ character, and a large number of band crossings are visible here in the constant energy maps of panels (d), (h), and (l).

While previous ARPES works on $Sr_3Ir_2O_7$ have primarily used the reduced Brillouin zone delineated by the orange boundaries in these figures, two features seemingly align more closely with the green zone boundaries of the unreduced Brillouin zone. The first is the difference between the spectra near the Γ and Γ′ points, especially visible at a binding energy of 400 meV in the $x = 3.5\%$ sample in Fig. 2(g) [and to a lesser extent in the $x = 6\%$ sample, Fig. 2(k)]. In each, a large pocket is observed at Γ′ and only faint spectral weight related to a deeper band maximum is visible at Γ, though this may be related to photoemission matrix element effects at normal emission as seen in undoped $Sr_3Ir_2O_7$ [9]. The second is the elongation of the lower Hubbard band pockets along the $\Gamma' - X$ direction in the $x = 1\%$ and $x = 3.5\%$ samples and, to a lesser degree, along the $\Gamma - X$ direction in the $x = 6\%$ sample. In the case of the reduced (orange) Brillouin zone, these pockets should have fourfold rotational symmetry about the X point, with the same width along the $\Gamma - X$ and $\Gamma' - X$ directions, while these are not required by the unreduced (green) Brillouin zone. A similar distortion has been noted in undoped $Sr_3Ir_2O_7$ [27,29], with two distinct explanations that each depend on the incident photon energy. One study suggests that the bonding and antibonding bands have opposite elongations, so that the overall band structure is symmetric under the required rotation, but that a given photon energy

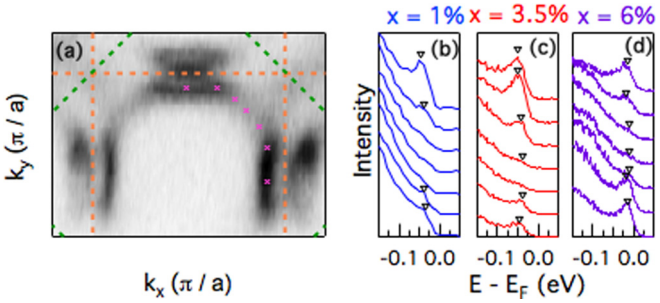

FIG. 3. Detailed evolution of M point band. (a) Fermi surface of the $x = 6\%$ sample in and near the first Brillouin zone. (b)–(d) EDCs taken along the arc in the $x = 6\%$ Fermi surface for the $x = 1\%$, $x = 3.5\%$, and $x = 6\%$ samples, respectively, at momentum locations marked by magenta stars in panel (a). (e)–(h) Zoomed in constant energy maps of the electronlike band in the region marked by a yellow rectangle in panel (a), from 10 meV above E_F to a binding energy of 40 meV near the band bottom.

will preferentially select one of these bands resulting in the observed elongation. The other explanation of the X point elongation comes from considering a bulk Brillouin zone in which the cross section of the first Brillouin zone at a particular k_z value is not a square. In particular, at $k_z = 0$ the point labeled Γ' here is actually the bulk Z point, and the Brillouin-zone boundary is naturally elongated along $\Gamma' - X$. Most published calculations of the band structure of $Sr_3Ir_2O_7$ do not consider this three-dimensional zone, and such calculations may be useful to determine the relevance of the bulk Brillouin zone for this system. We further note that there have been recent reports [30] showing broken symmetries in the structure of the Ir-O octahedra such that the correct lattice for $Sr_3Ir_2O_7$ is monoclinic rather than tetragonal, as the square BZ we use here would suggest. The distortions causing the system to depart from tetragonal symmetry are quite small (on the order of 0.1%), and thus should not be clearly visible in the ARPES spectra here.

While the primary change in the Fermi surface with increasing electron concentration is the increasing size of the nearly elliptical Fermi-surface pockets in the $x = 1\%$ sample, the geometry of these pockets also changes with doping. Notably, in the $x = 6\%$ sample, whose Fermi surface is replicated in Fig. 3(a), there is spectral weight at the Fermi level in a large arc between the pockets not observed in the lower doping levels. This is reflected in the energy distribution curves (EDCs) along this arclike feature at momentum locations marked by magenta stars in Fig. 3(a) shown in Figs. 3(b)–3(d). This arc is manifested by the small peak at E_F for the $x = 6\%$ sample for all momenta observed, and likely corresponds to dispersion of this band slightly above the chemical potential (as suggested in connection to a similar observation in Ref. [26]). Indeed, the peak positions are at a lower binding energy nearer the $\Gamma - X$ direction. As expected, no such residual peak is observed in the EDC along the $\Gamma - X$ direction in the $x = 1\%$ and $x = 3.5\%$ samples.

The width of the electron pocket along its long dimension is extracted from the separation of MDC peaks taken along the k_x direction at the widest part of the pocket, as indicated for the $x = 6\%$ sample by the magenta line in figure 4(a). These MDCs are shown in Fig. 4(d) for the $x = 1\%$, 3.5%, and 6% samples. The peak locations, obtained from a fit of two Gaussian peaks and constant background, are marked by magenta squares and grow significantly farther apart with additional doping, as shown by the evolution of the magenta trace in Fig. 4(g). The width of the pocket along the narrow direction is similarly extracted from MDCs along that direction (k_y for the pocket shown in the figure) and marked by orange circles. In each of these MDCs in Fig. 4(e), there are three distinct peaks rather than the four that would be expected from the two nearby pockets [one from each band crossing in this direction as shown in panels (a) and (c)] due to a combination of matrix element effects (like those seen in Ref. [25], especially notable in the $x = 3.5\%$ sample where the constant energy maps only faintly show one of the two pockets) and the nearness of the two inner Fermi-level crossings (especially important in the $x = 6\%$ sample). Further, these peaks are difficult to resolve above the noise level in the $x = 1\%$ and $x = 3.5\%$ samples, making the determination of the pocket width difficult. To this end, the error bars reported for this measurement in Fig. 4(g) are set by the width of the overall feature on one side of the Brillouin-zone boundary and these less-certain measurements are marked by lighter circles in Fig. 4(g). This width undergoes a more modest change with doping, increasing from $W_{\text{short}} = 0.04\,\pi/a$ at $x = 1\%$ to only $W_{\text{short}} = 0.09\,\pi/a$ at $x = 6\%$.

The band minima for these electronlike bands are offset in momentum from the M point. This offset is not predicted in LDA+SOC+U calculations for the single layer Sr_2IrO_4 compound and thus is likely related to the bilayer splitting in the system. This momentum offset can be measured in the separation between the two-band minima along the $\Gamma - M$ direction, extracted from MDC peak locations at the bottom of the conduction band. The binding energy at which these MDCs are taken is different for each doping, determined from the upturn of the EDC taken at the middle of the Fermi pocket. These MDCs are shown in Fig. 4(f) for the three dopings measured here, and the peak locations are marked with green triangles. Contrary to a rigid dopinglike picture, the band minima move farther apart with increasing doping.

The evolution of near-E_F band dispersions in $(Sr_{1-x}La_x)_3Ir_2O_7$ can be seen in the energy-momentum spectra along the high-symmetry directions shown in Fig. 5. The $M - \Gamma - X - M - \Gamma'$ path for each doping is denoted by the purple line in Fig. 2(a). Panels (a), (c), and (e) show the raw ARPES spectra, while panels (b), (d), and (f) depict the second derivative with respect to energy, commonly used to highlight band dispersions. As previously observed [22], the electronlike "conduction" band becomes more filled with increasing doping and moves toward the chemical potential as the low-energy spectral weight suppression vanishes. In the $x = 1\%$ sample, there are two features near the Fermi level at the X point: one at approximately 300 meV, in roughly the same place as observations of the lower Hubbard band in undoped $Sr_3Ir_2O_7$, and another near 100 meV, nearer the position of the lower Hubbard band in the more heavily doped samples. In the $x = 3.5\%$ sample, there is a stronger difference in the features observed at the Γ and Γ' points than that observed in the other samples, with a band at a binding energy near 500 meV at Γ and near a shallower band near

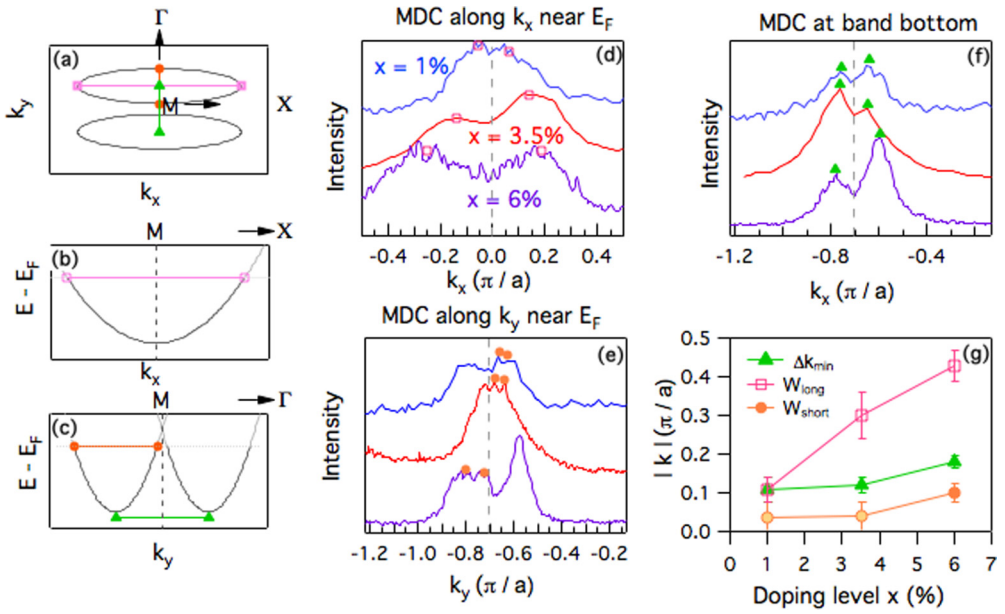

FIG. 4. Doping evolution of conduction-band parameters. (a) Cartoon Fermi surface illustrating the band parameters extracted from MDCs in panels (d)–(f). (b),(c) Cartoon dispersions along high-symmetry directions illustrating the same band parameters. (d) MDCs along the widest part of the Fermi-surface pocket for each sample at E_F, with magenta squares marking k_F locations. (e) MDCs along the middle of the Fermi-surface pocket in the narrower direction for each sample at E_F, with orange circles marking k_F locations. (f) MDCs along the same direction as in panel (f) at the binding energy of the minima of the electronlike pockets for each sample, with green triangles marking the momentum location of the band minima. (g) Doping evolution of the Fermi pocket dimensions and separation between band minima.

350 meV at Γ′. While this suggests some difference between Γ and Γ′, the separation between these bands is quite close to the bilayer splitting observed at the Γ point in the $x = 6\%$ sample, suggesting a correspondence between these bands and that photoemission matrix elements likely play a role in this discrepancy. Notably, the $x = 3.5\%$ measurements were taken at a different beamline with different experimental geometry than the other measurements, which could give rise to such matrix element effects. Allowing for these matrix elements, our data support the use of the bulk Brillouin zone, in which the Γ′ point is equivalent to the Z point and should be quite similar to Γ due to the minimal c-axis dispersion observed in this system.

The evolution of band separations can be more easily quantified via the analysis of energy distribution curves (EDCs) as in Fig. 6. In panels (a) and (b), we show the EDCs corresponding to the band maxima at X and Γ / Γ′, respectively, for each doping level measured here. In panel (c), we show EDCs corresponding to the momentum location of the band minimum near M, which changes slightly with doping (see discussion of Fig. 4). The upward movement of this band minimum near the M point with increasing doping is counter to a picture of rigid doping into an electron pocket and is due to the previously observed low-energy spectral weight suppression in the low doping regime [22]. The EDCs for this near-M band are qualitatively the same for each sample, while the number

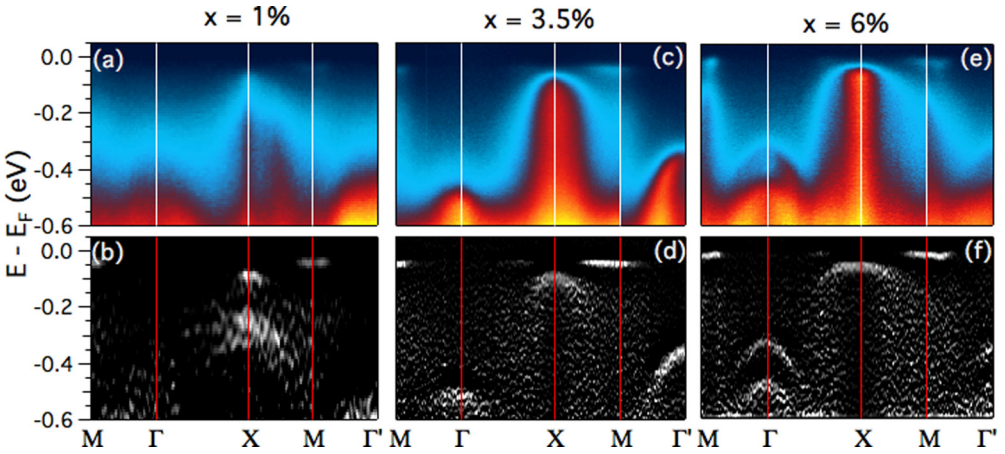

FIG. 5. Dispersion near the Fermi energy for $(Sr_{1-x}La_x)_3Ir_2O_7$ samples. (a) Raw ARPES spectrum for the $x = 1\%$ sample along a $M - \Gamma - X - M - \Gamma'$ path [marked in Fig. 2(a)]. (b) Second derivative with respect to energy of (a). (c)–(f) The same as (a) and (b) for the $x = 3.5\%$ and $x = 6\%$ samples.

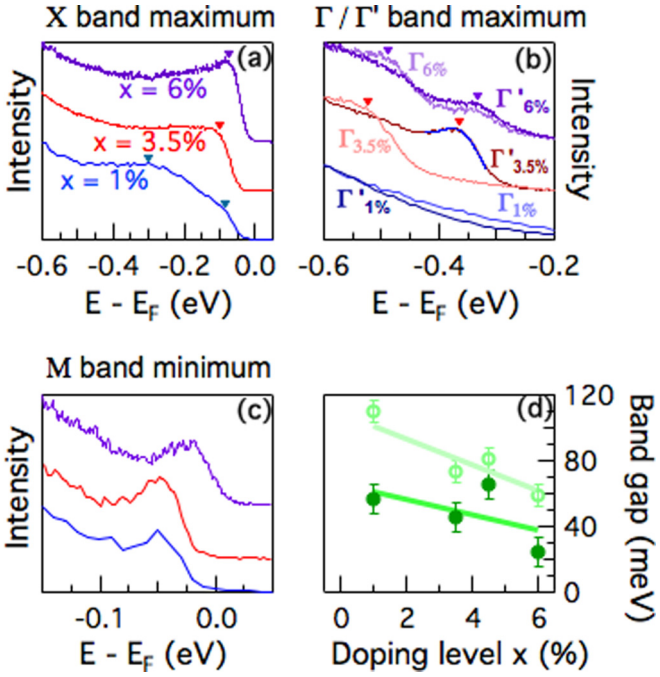

FIG. 6. Band extrema locations in $(Sr_{1-x}La_x)_3Ir_2O_7$. (a) EDCs at the X point through the maximum of the lower Hubbard band for the $x = 1\%$, $x = 3.5\%$, and $x = 6\%$ samples, with triangles marking the extracted feature locations. (b) EDCs at the Γ and Γ' points for the same samples. (c) EDCs through the band minima near the M point for the same samples. (d) Band gap extracted from the distance from the X point maximum to the M point minimum (dark circles) and from the X point maximum to E_F (light circles) as a function of doping.

of features visible in the X, Γ, and Γ' bands changes between samples.

From the EDCs taken at the X point in each sample [Fig. 6(a)], it appears that there is a transfer of spectral weight from the 300-meV feature to the 100-meV feature with increasing doping. There are two clearly visible distinct features in the $x = 1\%$ spectrum, a flat spectrum with a leading edge near 100 meV in the $x = 3.5\%$ measurement, and a more pronounced peak near 100 meV in the $x = 6\%$ sample. The peak at higher binding energy more closely matches the lower Hubbard band position in undoped $Sr_3Ir_2O_7$, especially considering the downward shift due to the introduction of electrons. This crossover from a high-energy feature to a low-energy feature at X, which has been observed in a previous ARPES study of $(Sr_{1-x}La_x)_3Ir_2O_7$ [25] (though at a different doping level), may be due either to the formation of an in-gap state or due to inhomogeneity in the doping level within the measured area. STM measurements of lightly doped $(Sr_{1-x}La_x)_3Ir_2O_7$ have revealed metallic regions within tens of nanometers of regions with a density of states that is fully gapped, well within the size of the beam spot used here [11,12]. This sample-dependent coexistence of metallic and insulating regions could explain the different doping level at which this spectral weight transfer occurs between the present study and the literature (in a previous study [25], this crossover is observed near a doping level of $x = 4\%$). As previously discussed, the separation between the two bands at the Γ point (or the band at Γ and the band at Γ' in the case of the $x = 3.5\%$ sample) is related to the bilayer splitting in the system. Published studies of the $x = 0\%$ compound show a splitting of 180 meV between these bands [9,27], while the splitting in both the $x = 3.5\%$ and $x = 6\%$ samples is 158 and 157 meV, respectively. The EDCs at the Γ and Γ' points in the $x = 1\%$ sample do not show clear peaks corresponding to these bands, and thus it is difficult to extract a precise value of this splitting. The difference between literature values for undoped $Sr_3Ir_2O_7$ and the doped samples here appears significant (though different handling of the spectral background in the literature may play a role), but no significant change is observed across the metal-insulator transition. Finally, the splitting between the bands at X ($J_{\text{eff}} = \frac{1}{2}$) and Γ/Γ' ($J_{\text{eff}} = \frac{3}{2}$) is $\approx$255 meV in the $x = 6\%$ sample and $\approx$265 meV in the $x = 3.5\%$ sample, indicating a highly similar but potentially weaker effect of spin-orbit coupling with increased doping.

One important doping-dependent quantity that can be extracted from the position of these bands is that of the Mott gap as a function of doping. This is related to the ambiguity in the origin of the conduction band at the M point. If this is the bottom of the upper Hubbard band, which is consistent with its momentum location in LDA+SOC+U calculations, then the Mott gap is the distance between the X point maximum and the near-M minimum. If, instead, the band at M is an in-gap state, then the Mott gap is somewhat larger and can be estimated by the distance from the band maximum at X to the chemical potential. The gap values implied by the data for these two scenarios are shown in Fig. 6(d), with dark (light) green circles marking the former (latter) explanation. Green lines provide guides to the eye for the trends of these gap values with doping. In either case, there is a net decrease in the gap magnitude over the doping range studied, with an increase across the metal-insulator transition between $x = 3.5\%$ and $x = 4.5\%$. This unexpected increase is well within the error bars for the lower Hubbard band–chemical potential gap, while much larger in the measured gap between the lower Hubbard band and the conduction band. This discrepancy largely comes from the vanishing of a 20-meV spectral weight suppression in the antiferromagnetic samples across the metal-insulator transition. This may indicate that the position of the lower Hubbard band is the better indicator of the Mott gap. This is in line with a previous study of $(Sr_{1-x}La_x)_3Ir_2O_7$, though our gap values are somewhat lower than those reported in that work [25]. The major part of this discrepancy is due to observation of the two bands at the X point. In that work, the lower binding energy band is not observed in samples below a doping level of $x = 5\%$. Both works agree that the gap remains open to high doping levels ($x \geqslant 6\%$), in contrast to the single-layer Sr_2IrO_4 where the Mott gap collapses abruptly [16].

The evolution of the effective mass in the lower Hubbard band and conduction band with doping is illustrated in Fig. 7. Band dispersions are determined by taking EDCs at each of several momentum points along a line in the Brillouin zone, and extracting a characteristic energy for each. As the lower Hubbard band lacks a clear peak feature in the $x = 1\%$ and $x = 3.5\%$ samples, the leading edge midpoint was taken as the band position, as shown in panels (a)–(c). Similar EDC stacks for the conduction band are shown in panels (f)–(h), where a

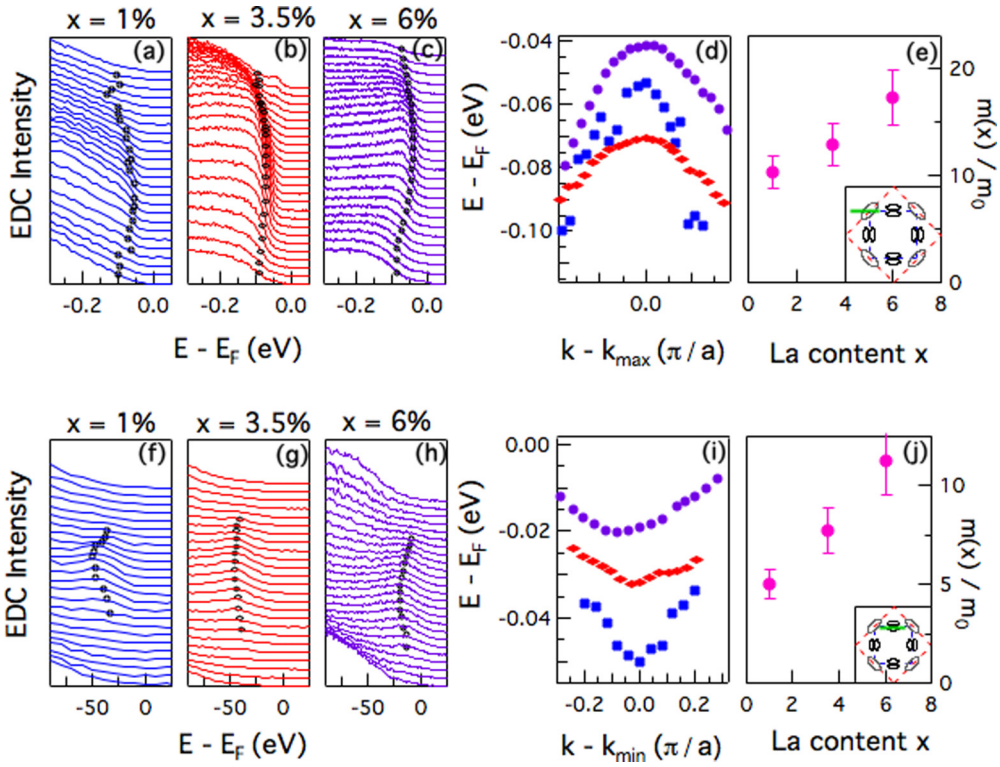

FIG. 7. Effective masses of lower Hubbard band. (a)–(c) EDCs taken at momentum positions along the $M - X$ direction [marked in inset to panel (e)] in the $x = 1\%$, 3.5%, and 6% samples. (d) Dispersions for the lower Hubbard band extracted from the EDC fits in (a)–(c). (e) Effective masses in $(Sr_{1-x}La_x)_3Ir_2O_7$ as a function of doping from the fits to dispersion. (f)–(j) The same as (a)–(e), for the conduction band rather than the lower Hubbard band.

peak position can be fit. Panels (d) and (i) show these extracted dispersions for each doping level, which are then fit near the band extremum with a quadratic band in which the effective mass is a parameter. These extracted masses are plotted in panels (e) and (j) as magenta circles, normalized by the free-electron mass m_0. Error bars are derived from statistical errors in the quadratic fits, combined with the variation in mass parameter acquired from shifting the fitting range near the extremum, accounting for both the noise in band positions and asymmetry apparent in the bands. The absolute values of these band masses are similar to those reported in some systems of doped $SrTiO_3$ [31]. Both bands display a similar increase of a factor of 2.5 between the $x = 1\%$ and $x \approx 8\%$ samples, evolving smoothly across the metal-insulator transition near $x = 4\%$. The high effective mass in metallic samples is in rough agreement with, though somewhat higher than, values from a recent work in which the mass enhancement is indirectly measured using infrared spectroscopy [15].

IV. DISCUSSION

Figure 8 compares the doping-dependent effective mass of the conduction band and lower Hubbard band of $(Sr_{1-x}La_x)_3Ir_2O_7$ with phenomena observed in cuprate superconductors, shown in Fig. 8(a). Since the bands in the cuprates are approximately half filled, the mass renormalization is extracted from linear fits to the dispersion near the chemical potential crossing rather than parabolic fits near band extrema as was done in $Sr_3Ir_2O_7$. Filled symbols correspond to the ratio of band velocities measured at binding energies $E_B \geqslant 100$ meV for three families of cuprate superconductors. This energy range is chosen to exclude explicit renormalization effects from electron-boson coupling which only impact states within an energy window of $E_b \approx \hbar\omega$ of the Fermi level. For all three cuprate families, the inverse band velocity, and thus the effective mass, increase with doping at roughly the same rate. This is in line with the observed change in effective mass

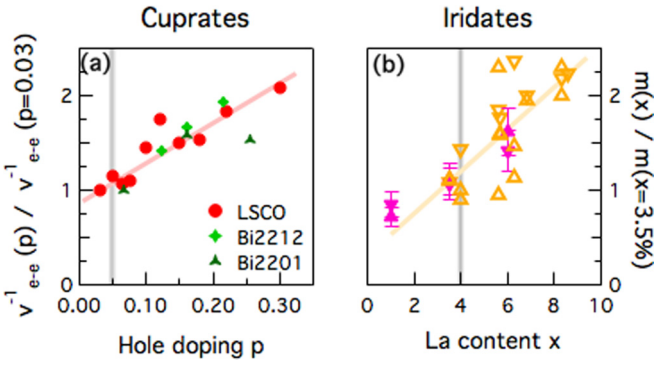

FIG. 8. Doping dependence of band renormalization in cuprates and iridates. (a) Doping dependence of band renormalization in $La_{2-x}Sr_xCuO_4$ (LSCO, red circles) $Bi_2Sr_2CaCu_2O_{8+\delta}$ (Bi2212, light green diamonds) and $Bi_2Sr_2CuO_{4+\delta}$ (Bi2201, dark green triangles) from [32]. (b) Doping dependence of effective mass in lower Hubbard band (downward pointing triangles) and conduction band (upward pointing triangles) in $(Sr_{1-x}La_x)_3Ir_2O_7$, from Figs. 7 and 8.

in $(Sr_{1-x}La_x)_3Ir_2O_7$, suggesting a connection between the change in effective mass with doping observed in the iridates to this high-energy renormalization observed in cuprates. In cuprates, this slope change has been associated with a "high-energy anomaly" wherein the band velocity drastically changes at an energy between 0.3 and 0.5 eV [33,34]. A similar anomaly is present at high energy (near 1 eV) in Sr_2IrO_4 [35], though no such feature has been reported in $Sr_3Ir_2O_7$. In studies with data at sufficiently high binding energy [9,27] the ARPES spectra become broad near 1 eV, making the detailed study of dispersions at this binding energy difficult. This type of feature is thought to be a manifestation of strong correlations, though its doping dependence does run counter to the basic picture of mass increasing with strengthening correlations [34,36].

V. CONCLUSION

Despite the many energy scales relevant in the ground state of $(Sr_{1-x}La_x)_3Ir_2O_7$, the primary effects on the band structure with doping in the portion of the phase diagram observed here can be understood in terms of electron-electron correlations. Other than the previously reported spectral weight suppression at low doping, all of these changes evolve smoothly across the metal-insulator transition at $x \approx 4\%$. The Mott gap weakens but does not close over the observed doping range, signaling a weakening of the role of on-site Coulomb correlations as itinerant electrons are introduced. The valence and conduction bands both show an anomalous effective mass enhancement as these correlations weaken, in parallel with the high-energy anomaly observed in a variety of cuprate superconductors. These similarities, along with the small change in the splitting due to spin-orbit coupling and negligible effect of bilayer coupling suggest that electron-electron correlations and associated Mott physics are primarily responsible for the doping-dependent changes in $(Sr_{1-x}La_x)_3Ir_2O_7$.

ACKNOWLEDGMENTS

This work was primarily funded by the US Department of Energy, Office of Science, Office of Basic Energy Sciences, Materials Sciences and Engineering Division under Contract No. DE-AC02-05-CH11231 (Quantum materials KC2202) (G.A. and A.L.). Support was also provided by NSF Award No. DMR 1505549 (S.D.W. and T.H.).

[1] B. J. Kim, H. Jin, S. J. Moon, J.-Y. Kim, B.-G. Park, C. S. Leem, J. Yu, T. W. Noh, C. Kim, S.-J. Oh, J.-H. Park, V. Durairaj, G. Cao, and E. Rotenberg, Phys. Rev. Lett. **101**, 076402 (2008).

[2] S. Boseggia, R. Springell, H. C. Walker, A. T. Boothroyd, D. Prabhakaran, D. Wermeille, L. Bouchenoire, S. P. Collins, and D. F. McMorrow, Phys. Rev. B **85**, 184432 (2012).

[3] S. Chikara, D. Haskel, J. H. Sim, H. S. Kim, C. C. Chen, G. Fabbris, L. S. I. Veiga, N. M. Souza-Neto, J. Terzic, K. Butrouna, G. Cao, M. J. Han, and M. van Veenendaal, Phys. Rev. B **92**, 081114 (2015).

[4] J. Kim, A. H. Said, D. Casa, M. H. Upton, T. Gog, M. Daghofer, G. Jackeli, J. van den Brink, G. Khaliullin, and B. J. Kim, Phys. Rev. Lett. **109**, 157402 (2012).

[5] O. B. Korneta, T. Qi, S. Chikara, S. Parkin, L. E. De Long, P. Schlottmann, and G. Cao, Phys. Rev. B **82**, 115117 (2010).

[6] S. J. Moon, H. Jin, K. W. Kim, W. S. Choi, Y. S. Lee, J. Yu, G. Cao, A. Sumi, H. Funakubo, C. Bernhard, and T. W. Noh, Phys. Rev. Lett. **101**, 226402 (2008).

[7] T. F. Qi, O. B. Korneta, S. Chikara, M. Ge, S. Parkin, L. E. De Long, P. Schlottmann, and G. Cao, J. Appl. Phys. **109**, 07D906 (2011).

[8] C. H. Sohn, M.-C. Lee, H. J. Park, K. J. Noh, H. K. Yoo, S. J. Moon, K. W. Kim, T. F. Qi, G. Cao, D.-Y. Cho, and T. W. Noh, Phys. Rev. B **90**, 041105 (2014).

[9] Q. Wang, Y. Cao, J. A. Waugh, S. R. Park, T. F. Qi, O. B. Korneta, G. Cao, and D. S. Dessau, Phys. Rev. B **87**, 245109 (2013).

[10] D. A. Zocco, J. J. Hamlin, B. D. White, B. J. Kim, J. R. Jeffries, S. T. Weir, Y. K. Vohra, J. W. Allen, and M. B. Maple, J. Phys.: Condens. Matter **26**, 255603 (2014).

[11] T. Hogan, Z. Yamani, D. Walkup, X. Chen, R. Dally, T. Z. Ward, M. P. M. Dean, J. Hill, Z. Islam, V. Madhavan, and S. D. Wilson, Phys. Rev. Lett. **114**, 257203 (2015).

[12] Y. Okada, D. Walkup, H. Lin, C. Dhital, T.-R. Chang, S. Khadka, W. Zhou, H.-T. Jeng, M. Paranjape, A. Bansil, Z. Wang, S. D. Wilson, and V. Madhavan, Nat. Mater. **12**, 707 (2013).

[13] Y. Kim, N. Sung, J. Denlinger, and B. Kim, Nat. Phys. **12**, 37 (2016).

[14] Y. K. Kim, O. Krupin, J. D. Denlinger, A. Bostwick, E. Rotenberg, Q. Zhao, J. F. Mitchell, J. W. Allen, and B. J. Kim, Science **345**, 187 (2014).

[15] G. Ahn, S. J. Song, T. Hogan, S. D. Wilson, and S. J. Moon, Sci. Rep. **6**, 32632 (2016).

[16] A. de la Torre, S. M. Walker, F. Y. Bruno, S. Riccó, Z. Wang, I. G. Lezama, G. Scheerer, G. Giriat, D. Jaccard, C. Berthod, T. K. Kim, M. Hoesch, E. C. Hunter, R. S. Perry, A. Tamai, and F. Baumberger, Phys. Rev. Lett. **115**, 176402 (2015).

[17] Y. J. Yan, M. Q. Ren, H. C. Xu, B. P. Xie, R. Tao, H. Y. Choi, N. Lee, Y. J. Choi, T. Zhang, and D. L. Feng, Phys. Rev. X **5**, 041018 (2015).

[18] Y. Cao, Q. Wang, J. A. Waugh, T. J. Reber, H. Li, X. Zhou, S. Parham, S.-R. Park, N. C. Plumb, E. Rotenberg, A. Bostwick, J. D. Denlinger, T. Qi, M. A. Hermele, G. Cao, and D. S. Dessau, Nat. Commun. **7**, 11367 (2016).

[19] J. W. Kim, Y. Choi, J. Kim, J. F. Mitchell, G. Jackeli, M. Daghofer, J. van den Brink, G. Khaliullin, and B. J. Kim, Phys. Rev. Lett. **109**, 037204 (2012).

[20] L. Li, P. P. Kong, T. F. Qi, C. Q. Jin, S. J. Yuan, L. E. DeLong, P. Schlottmann, and G. Cao, Phys. Rev. B **87**, 235127 (2013).

[21] X. Lu, D. E. McNally, M. M. Sala, J. Terzic, M. H. Upton, D. Casa, G. Ingold, G. Cao, and T. Schmitt, Phys. Rev. Lett. **118**, 027202 (2017).

[22] G. Affeldt, T. Hogan, C. L. Smallwood, T. Das, J. D. Denlinger, S. D. Wilson, A. Vishwanath, and A. Lanzara, Phys. Rev. B **95**, 235151 (2017).

[23] H. Chu, L. Zhao, A. de la Torre, T. Hogan, S. D. Wilson, and D. Hsieh, Nat. Mater. **16**, 200 (2017).

[24] J. He, T. Hogan, T. R. Mion, H. Hafiz, Y. He, J. D. Denlinger, S.-K. Mo, C. Dhital, X. Chen, Q. Lin, Y. Zhang, M. Hashimoto,

H. Pan, D. H. Lu, M. Arita, K. Shimada, R. S. Markiewicz, Z. Wang, K. Kempa, M. J. Naughton *et al.*, Nat. Mater. **14**, 577 (2015).

[25] J. He, H. Hafiz, T. R. Mion, T. Hogan, C. Dhital, X. Chen, Q. Lin, M. Hashimoto, D. H. Lu, Y. Zhang, R. S. Markiewicz, A. Bansil, S. D. Wilson, and R.-H. He, Sci. Rep. **5**, 8533 (2015).

[26] A. de la Torre, E. C. Hunter, A. Subedi, S. M. Walker, A. Tamai, T. K. Kim, M. Hoesch, R. S. Perry, A. Georges, and F. Baumberger, Phys. Rev. Lett. **113**, 256402 (2014).

[27] L. Moreschini, S. Moser, A. Ebrahimi, B. D. Piazza, K. S. Kim, S. Boseggia, D. F. McMorrow, H. M. Rønnow, J. Chang, D. Prabhakaran, A. T. Boothroyd, E. Rotenberg, A. Bostwick, and M. Grioni, Phys. Rev. B **89**, 201114 (2014).

[28] J.-M. Carter and H.-Y. Kee, Phys. Rev. B **87**, 014433 (2013).

[29] C. Liu, S.-Y. Xu, N. Alidoust, T.-R. Chang, H. Lin, C. Dhital, S. Khadka, M. Neupane, I. Belopolski, G. Landolt, H.-T. Jeng, R. S. Markiewicz, J. H. Dil, A. Bansil, S. D. Wilson, and M. Z. Hasan, Phys. Rev. B **90**, 045127 (2014).

[30] T. Hogan, L. Bjaalie, L. Zhao, C. Belvin, X. Wang, C. G. Van de Walle, D. Hsieh, and S. D. Wilson, Phys. Rev. B **93**, 134110 (2016).

[31] W. Wunderlich, H. Ohta, and K. Koumoto, Physica B **404**, 2202 (2009).

[32] X. J. Zhou, Y. Yoshida, A. Lanzara, P. V. Bogdanov, S. A. Kellar, K. Shen, H. Eisaki, and Z.-X. Shen, Nature (London) **423**, 398 (2003).

[33] J. Graf, G. H. Gweon, K. McElroy, S. Y. Zhou, C. Jozwiak, E. Rotenberg, A. Bill, T. Sasagawa, H. Eisaki, S. Uchida, H. Takagi, D. H. Lee, and A. Lanzara, Phys. Rev. Lett. **98**, 067004 (2007).

[34] W. Meevasana, X. J. Zhou, S. Sahrakorpi, W. S. Lee, W. L. Yang, K. Tanaka, N. Mannella, T. Yoshida, D. H. Lu, Y. L. Chen, R. H. He, H. Lin, S. Komiya, Y. Ando, F. Zhou, W. X. Ti, J. W. Xiong, Z. X. Zhao, T. Sasagawa, T. Kakeshita *et al.*, Phys. Rev. B **75**, 174506 (2007).

[35] Y. Liu, L. Yu, X. Jia, J. Zhao, H. Weng, Y. Peng, C. Chen, Z. Xie, D. Mou, J. He, X. Liu, Y. Feng, H. Yi, L. Zhao, G. Liu, S. He, X. Dong, J. Zhang, Z. Xu, C. Chen *et al.*, Sci. Rep. **5**, 13036 (2015).

[36] B. Moritz, S. Johnston, and T. Devereaux, J. Electron Spectrosc. Relat. Phenom. **181**, 31 (2010).